Molecular Dynamics Simulations of the Diffusion of Small Chain Hydrocarbons in 8-Ring Zeolites

ARTICLE *in* THE JOURNAL OF PHYSICAL CHEMISTRY C · FEBRUARY 2011

Impact Factor: 4.77 · DOI: 10.1021/jp102262n

3 AUTHORS, INCLUDING:

Aldo Fabrizzio Combariza Montañez
Universidad de Sucre
19 PUBLICATIONS **96** CITATIONS
SEE PROFILE

German Sastre
Research Scientist
118 PUBLICATIONS **2,367** CITATIONS
SEE PROFILE

Molecular Dynamics Simulations of the Diffusion of Small Chain Hydrocarbons in 8-Ring Zeolites†

Aldo F. Combariza, German Sastre,* and Avelino Corma*

Instituto de Tecnología Química, Universidad Politécnica de Valencia, Consejo Superior de Investigaciones Científicas, Av de Los Naranjos S/N, 46022 Valencia, Spain

Received: March 12, 2010; Revised Manuscript Received: August 23, 2010

Molecular dynamics (MD) simulations were performed to study the microscopic motion of methane, ethane, propene, and propane adsorbed in three pure silica zeolites with windows made of 8 SiO_4 tetrahedral units: Si-LTA, Si-IHW, and Si-ITE. The zeolite framework and guest structures have been simulated allowing full flexibility, using the well-known BKS model and the potential of Oie et al., respectively. The MD approach followed allows us to calculate the intra- and intercage dynamics of the smaller adsorbates, that is, methane and ethane, in statistically meaningful time and length scales in the temperature range studied, whereas for the larger size guest molecules the analysis of intercage motion is limited to higher temperatures. Calculated self-diffusion coefficients for methane, ethane, and propene show a decreasing trend correlated with increasing guest kinetic diameter sizes and decreasing critical window size, confirming experimental measurements on the molecular sieving properties of 8-ring zeolite frameworks. The microscopic motion of propane diffusing in Si-ITE suggests a somewhat anomalous diffusion process, which can be related to the levitation effect. Thus, guest diffusion translational motion is shown to be highly influenced by the topological features of the framework, with the dimensionality of the diffusion path exerting the most noticeable influence. The microscopic understanding of the host−guest dynamics can be used to highlight the trade-off between propane/propylene selectivity and diffusional differentiation in these materials.

Introduction

Zeolites are microporous crystalline materials extensively used in a wide set of industrial applications due to special characteristics like large free volume, low density, void spaces in the form of cages and channels, thermal stability, and acid/base properties.[1] Catalysis, adsorption,[2] ion exchange, electronics,[3] molecular sieving, and many other interesting applications are now common fields of application for these materials, and efforts are made to synthesize zeolites with extra large pores[4] as well as small pore zeolites with 8 SiO_4 tetrahedral units (8-ring) windows. Zeolites with cages and channels separated by 8-ring windows have been recognized as potential candidates for the entropic separation of hydrocarbons with sizes close to the 8-ring window aperture.[5–8] Materials recently synthesized such as ITQ-3,[6] ITQ-12,[7] and ITQ-32[9] allow the molecular sieving of hydrocarbons with similar kinetic diameters. Even more outstanding is its ability of separate mixtures of olefins and paraffins,[10] which was not possible with cation containing zeolites due to olefin oligomerization, which in turn causes the blocking of the zeolites. By cautiously choosing a particular structural type, it is possible to enhance the selectivity of a given separation process based on structural and topological influences on the dynamics of the adsorbates, as in the kinetically driven pressure swing adsorption (PSA) separation.

In the present work, we report results from molecular dynamics (MD) on the molecular motion of methane, ethane, propane, and propene adsorbed in three different all-silica 8-ring zeolites. One of our objectives is to gain insights into the temperature dependence of the molecular mobility of the guest phase adsorbed in 8-ring zeolites. We have chosen the following pure silica 8-ring zeotypes: LTA,[11] ITE,[8] and IHW.[9] The main advantage in studying dynamics of adsorbates within pure silica zeolites comes from the lack of complicated interactions coming from counterbalancing cations, thus allowing only topological and structural features to influence the motion of the guest phase. From the selected structures, all-silica LTA (zeolite ITQ-29) is probably the most studied one, both computationally[12–17] and experimentally,[18–21] due to its highly symmetric cubic lattice of nearly spherical cages connected through 8-ring windows.[11] Si-LTA structure is thus a good candidate to test the performance of the simulation approach with existing experimental and computational information. Adsorption and diffusion properties of short chain hydrocarbons in all-Si ITE (zeolite ITQ-3) and all-Si IHW (zeolite ITQ-32)[8] have been recently studied,[6,22] focusing primarily on the simulation of adsorption isotherms. Our main purpose is to extend previous studies[23] by looking at the short- and long-range microscopic features of the diffusants which could be used to screen potential candidates for entropic separations.

Zeolite Models

We have selected three pure silica zeolites of framework type LTA, IHW, and ITE. Table 1 and Figure 1 provide details of the different zeolite structures used in the calculations: lattice parameters, volumes, simulation cell size, number of atoms in the simulation cell, and dimensionality.

Zeolite ITQ-29 (all silica LTA framework type) can be seen as a three-dimensional network of spherical cavities (alpha-cages), of about 11.4 Å in length, interconnected by six small 8-ring windows with an effective diameter of 4.1 Å.[11] Likewise, all silica LTA can be described as a structure made of sodalite

† Part of the "Alfons Baiker Festschrift".

* To whom correspondence should be addressed. E-mail: gsastre@itq.upv.es (G.S.); acorma@itq.upv.es (A.C.).

10.1021/jp102262n
Published on Web 09/23/2010

TABLE 1: Pure Silica Zeolites: Lattice Parameters and Cell Volume

zeolite	a (Å)	b (Å)	c (Å)	$\alpha = \beta = \gamma$ (deg)	vol (Å^3)	sim. cell.	atoms	dimensionality
(ITQ-29) LTA[11]	11.92	11.92	11.92	90.0	1693.2	2 × 2 × 2	576	3D
(ITQ-32) IHW[9]	13.70	24.02	18.20	90.0	6064.6	2 × 1 × 1	672	2D
(ITQ-3) ITE[8]	20.75	9.80	20.01	90.0	4071.1	2 × 2 × 1	768	2D (pseudo 1D)

cages (beta-cages) connected through the square faces with each other, forming double four-ring units. The diffusion path in this zeolite involves the three crystallographic axis. The pore topology of ITQ-32 zeolite features a unidirectional small 8-ring channel system along the crystallographic *a* axis, with a pore aperture of 3.5 × 4.3 Å. The 8-ring pore system is perpendicularly crossed by relatively short 12-ring channels, which interconnect two neighbored 8-ring channels along the *c* direction. These bridged 12-ring channels have a diameter of 6.3 and 16.2 Å in length.[9] ITQ-32 has been the object of several experimental studies for adsorption and separation of olefins from paraffins, which highlights the potential of this structure for the kinetic separation of similar sized molecules, as is the case of propane/propene.[5] ITQ-3 zeolite (ITE framework type) is a structure formed by a bidimensional network of straight channels connected by 8-ring windows running along the *b* and *c* crystallographic axis, with space group symmetry *Cmcm* in an orthorhombic unit cell. The intersection of both types of channels generates four large cavities per unit cell, with two different 8-ring windows with different opening sizes.[8] The marked difference in window openings in this material (see Figure 1) only allows the diffusion of hydrocarbons along the *b* crystallographic axis, thus becoming a pseudo-one-dimensional arrangement of interconnected cages. This zeolite has also been the object of experimental studies due to its ability to adsorb small hydrocarbons, and its potential for molecular sieving processes has been recognized by the differences in adsorption rates for propane and propene.[6]

TABLE 2: Critical Diameters for Methane, Ethane, Propene, and Propane[a]

	critical diameters (Å)		
structures	LX	LY	LZ
propane	4.0	4.5	6.6
propene	4.0	4.2	6.6
ethane	3.8	4.1	4.8
methane	3.8	4.1	3.9

[a] LX, LY, and LZ refer to the length of the shadow resulting from the projection of the molecules with respect to the planes XZ, XY, and YZ, respectively.[25]

All zeolites described above feature 8-ring windows connecting either channels or cages, but the configurations of the connecting windows differ as a consequence of each specific topology. The intrinsic angles SiOSi−OSiO and dihedral SiOSiO define the window shapes and sizes. The values of the window openings are taken according to the oxygen van der Waals radii 1.35 Å recommended by the IZA.[24] For comparison, we have calculated kinetic diameters for ethane, ethylene, propane, propylene, and methane according to the approach developed by Rohrbaugh and Jurs.[25] The data is shown in Table 2, and a schematic representation of the guest molecules is given in Figure 2.

Methods

Computational Details. We have used MD to simulate the intracage and intercage motion of methane, ethane, propane,

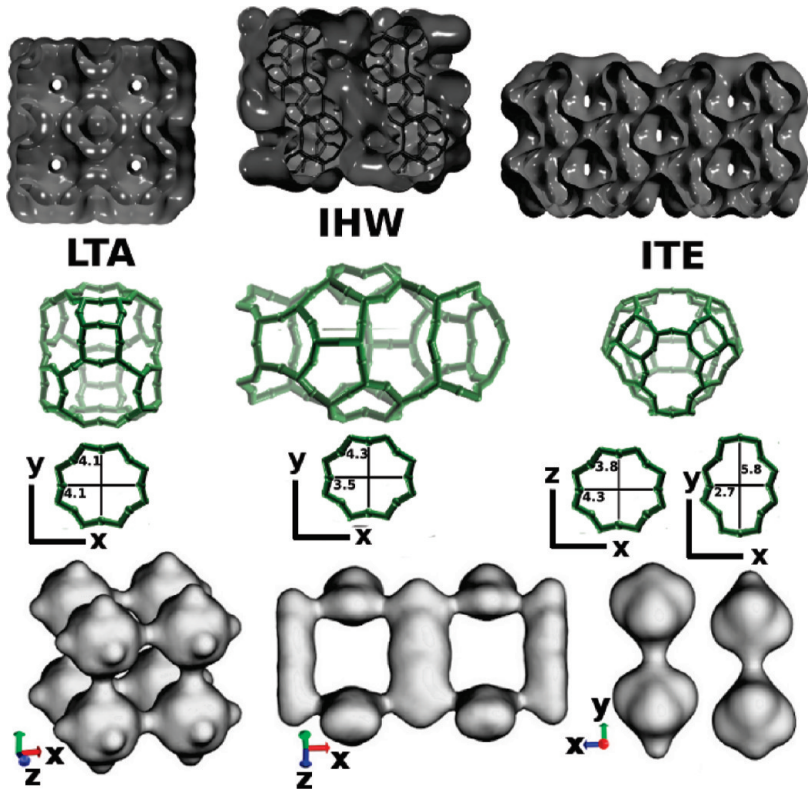

Figure 1. Schematic representation of occupancy volume maps (up), cages, channels, and window sizes (middle), and volume maps (down) from the probability density of CH_4 inside the model zeolite structures.

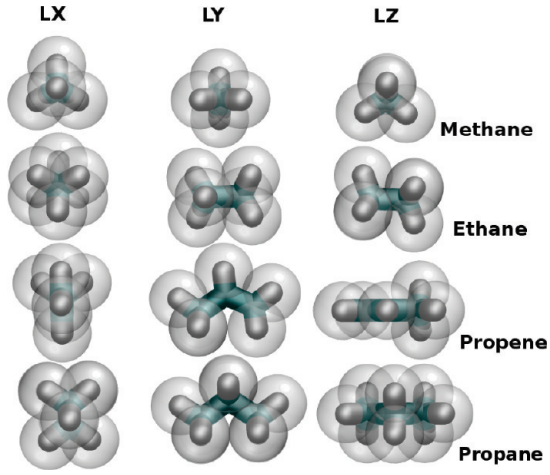

Figure 2. Schematic representation of methane, ethane, propene, and propane along the x, y, and z axes.

and propene adsorbed in pure silica framework types using the parallel general purpose DL_POLY_2.20 code.[26] Full framework/guest flexibility has been included in the MD calculations, as framework flexibility has been recognized to have a big impact on the short- and long-range dynamics of adsorbates in nanoporous materials.[27,28] We have used the NVE ensemble for MD calculations and histogram sampling for the probability density calculations.[29,30] Simulation cells are generated by appropriate scaling of the unit cells, as shown in Table 1. The velocity-Verlet algorithm is used throughout to integrate the Newton's equations of motion with a time step of 1 fs. The loading is set to four guest molecules per simulation cell for all systems. The low guest loading was chosen to ensure that guest inter-intracage mobility is not controlled by adsorbate−adsorbate interactions.

All systems sample the NVE ensemble, with temperatures of 300, 600, 900, and 1200 K. Trajectories were equilibrated for at least 150 ps, a time range in which velocities are scaled every 5 fs to the target temperature. Preproduction runs are then initiated up to 200 ps, or until no statistically meaningful variation of total energy was reached. Production runs were initiated from these equilibrated systems, with simulation times going from 10 ns for methane up to 100 ns for propane and propylene. Analysis of the trajectories is carried out from the history files generated. Intracrystalline self-diffusion constants were obtained from the Einstein relation

$$2tD = \frac{1}{N_t}\langle |r(t + t_0) - r(t)|^2 \rangle \quad (1)$$

where r is the guest center of mass position vector, N_t is the number of translational degrees of freedom of the guest molecule, and the symbol denotes the ensemble average. The factor N_t therefore depends on the dimensionality of the framework (see Table 1 and Figure 1) and is defined as $N_t^{LTA} = 3$, $N_t^{HW} = 2$, and $N_t^{TE} = 1$ for the different frameworks. From the self-diffusion coefficients obtained at the different temperatures, it is possible to estimate the Arrhenius activation energy from the following relation:

$$D = D_0 \exp\left[-\frac{E_a}{RT}\right] \quad (2)$$

TABLE 3: BKS Forcefield Parameters

Si (e)	+2.4
O (e)	−1.2
A_{Si-O} (eV)	18003.7572
A_{O-O} (eV)	1388.7730
ρ_{Si-O} (Å)	0.205205
ρ_{O-O} (Å)	0.362319
C_{Si-O} (eV Å^6)	133.5381
C_{O-O} (eV Å^6)	175.0000

where R is the gas constant, T is the temperature, and E_a is the activation energy. However, our calculations show that the linearity, and thus the validity of the Arrhenius behavior, is not comprehensive over the whole range of temperatures (*vide infra*). Thus, the values of activation energy calculated with eq 2 should only be seen as a qualitative result.

Potential Energy Surface. The potential energy surface of the system takes into account three main terms: the zeolite potential energy, V^{Zeo}, the guest potential energy, V^{Guest}, and the intermolecular potential energy contribution, $V^{Zeo-Guest/Guest-Guest}$.

$$V^{Total} = V^{Zeo} + V^{Guest} + V^{Zeo-Guest/Guest-Guest} \quad (3)$$

The potential energy of the framework was represented in the following way: a Coulombic part accounting for the long-range electrostatic interactions and a short-range two-body function which models the repulsion and the dispersion energy between close pairs (see eq 4).

$$V^{Zeo} = V^{Zeo-Short} + V^{Zeo-Coul} \quad (4)$$

To evaluate the Coulomb sum ($V^{Zeo-Coul}$), we have used the particle mesh Ewald formalism.[31] For the short-range interactions ($V^{Zeo-Short}$), we have chosen the well-known Born−Mayer model for ionic solids of van Beest et al. (BKS).[32] The BKS potential is applied only to oxygen−oxygen and oxygen−silica pair interactions. This potential (see eq 5 and parameters in Table 3) is divided into two terms: a repulsive contribution, given by the exponential term, and an attractive-dispersive one. This formulation allows a treatment of the interactions among the atoms as simply and physically reasonable as possible, for both short- and medium-range distances.

$$V_{BKS}^{Zeo-Short} = A_{ij} \exp\left(\frac{-r_{ij}}{\rho_{ij}}\right) - \frac{C_{ij}}{r^6} \quad (5)$$

The intramolecular potential for the hydrocarbons comprises two-body (bond), three-body (angle), and four-body (dihedral) interactions plus the electrostatic Coulomb term. Parameters are given in the original reference by Oie et al.[33] Finally, Lennard-Jones (LJ) potentials are used to describe the intermolecular host−guest and guest−guest interactions. The 12−6 LJ functional form was used. The full set of parameters and a full description of the potentials can be obtained from the original references.[34,35]

Results and Discussion

Si-LTA Host−Guest Dynamics. Mean squared displacements at different temperatures for methane, ethane, propene, and propane adsorbed in Si-LTA are reported in Figure 3, and self-diffusion D_s coefficients calculated using the Einstein relation are presented in Table 4. The overall effect of

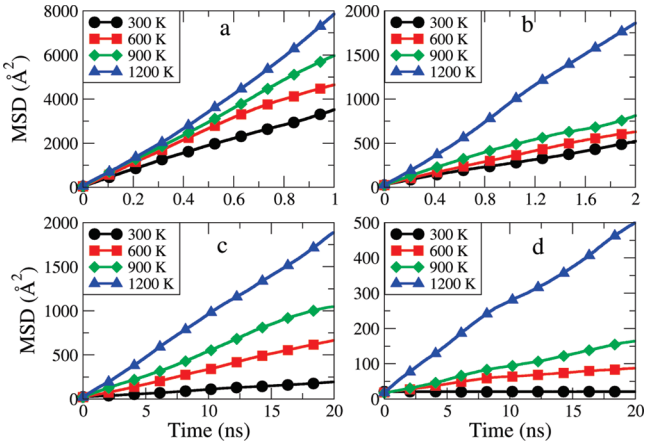

Figure 3. MSD plots for (a) methane, (b) ethane, (c) propene, and (d) propane adsorbed in Si-LTA zeolite at various temperatures.

TABLE 4: Experimental and Calculated Self-Diffusion Coefficients for Methane, Ethane, Propene, and Propane in All Silica LTA Zeolite[a]

	diffusion coefficients D_s (m²/s)			
temp (K)	CH_4	C_2H_6	C_3H_6	C_3H_8
300	5.9×10^{-9}	4.8×10^{-10}	1.4×10^{-11}	
600	6.1×10^{-9}	4.3×10^{-10}	5.6×10^{-11}	4.0×10^{-12}
900	9.5×10^{-9}	6.6×10^{-10}	9.1×10^{-11}	1.6×10^{-11}
1200	1.5×10^{-8}	1.7×10^{-9}	1.5×10^{-10}	3.8×10^{-11}
	[b] 3.0×10^{-10}	[f] 1.0×10^{-11} 1.0×10^{-7}	[d] 4.7×10^{-15}	[h] 1.5×10^{-12}
	[c] 1.0×10^{-9} [d] 1.4×10^{-10} [e] 1.0×10^{-9}	[d] 2.09×10^{-10} [e] 1.2×10^{-10}	[g] 5.0×10^{-14}	[e] 2.0×10^{-14}

[a] Top: Results from the present study. Bottom: Data from previous MD and experimental values. [b] MD 300 K(ref 34), [c] MD 300 K(ref 13), [d] Exp 300 K(ref 13), [e] MD 600 K(ref 13), [f] Exp 300 K(ref 18), [g] Exp 300 K(ref 19), [h] dcTST 600 K(ref 16).

temperature in the long-range displacement of the guest phase is an increase in MSD slopes. However, the length of the intercage motion is strongly dependent on the size of the adsorbate. Methane MSDs fluctuate from 4000 Å² to more than 10000 Å² in the temperature and time ranges represented in Figure 3, showing a highly linear MSD dependence which is a good indicator of the unhindered three-dimensional motion of the guest inside the porous system. The length of the MSDs also points to a diffusion process spanning over multiple cages, which allows the calculation of diffusion coefficients with high statistical certainty. The obtained diffusion coefficients are in good agreement with experimental values obtained recently by Hedin et al.[20] and with previously calculated diffusion coefficients obtained via MD.[16,13,36] The MSD landscape changes somewhat drastically when the diffusant size increases. Ethane MSDs range between ~400 Å² at 300 K up to ~1400 Å² at 1200 K in the time scale of Figure 3. As in the case of methane, ethane MSDs have an increasingly positive slope, highly linear, which indicates the ability of the diffusant to cross the entropic barriers presented at the windows of the connecting cages. Interestingly, there is an increasing gap between MSDs as the temperature increases, which shows a non-Arrhenius behavior of the diffusing guest at high temperature. This behavior is confirmed in the plot presented in Figure 4, which also shows a nonlinear dependence of the diffusion coefficient and temperature for methane. The activation energy for methane and ethane is very low with values of a few kJ/mol.

Propene MSDs depicted in Figure 3 show highly constrained intercage dynamics, with displacements limited to intracage

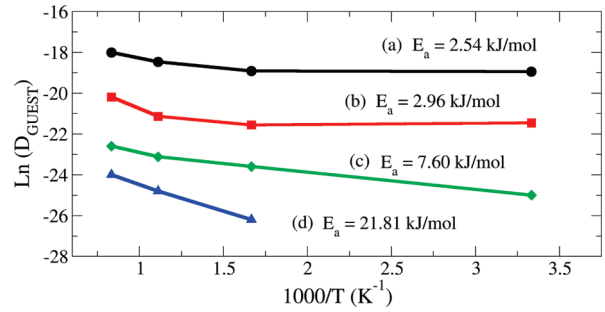

Figure 4. Arrhenius plots showing activation energies for (a) methane, (b) ethane, (c) propene, and (d) propane adsorbed in Si-LTA zeolite.

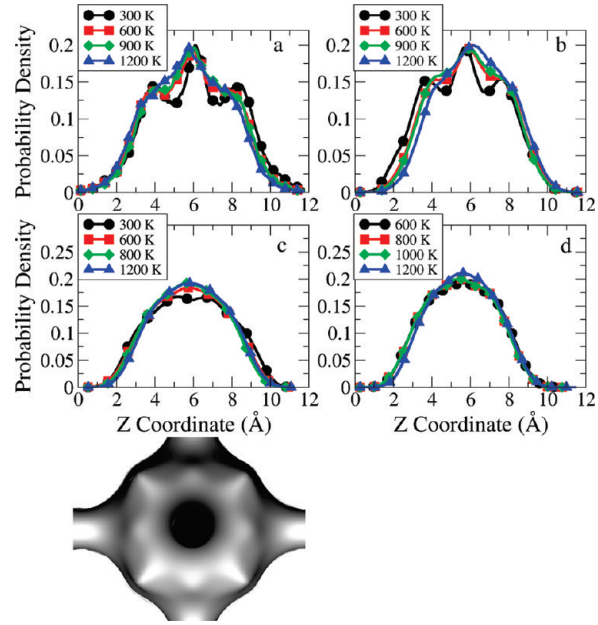

Figure 5. One-dimensional probability density distribution along the z axis for (a) methane, (b) ethane, (c) propylene, and (d) propane center of mass in Si-LTA zeolite, and its evolution with temperature. The LTA cavity (bottom) at the same scale is depicted.

motion at the lower temperature of 300 K, in the time range of the figure. Higher temperature dynamics start sampling beyond the cage-to-cage length only at 800 K, as is shown in the time scale depicted. However, diffusion coefficients and subsequent Arrhenius plots were calculated using long runs with at least 300 Å² MSDs. Propane shows almost negligible intercage motion at 300 K, with thermal excitation having an effect on diffusivity at the higher simulation temperatures. It is also noticeable that the time range represented in Figure 3 (i.e., 1−6 ns) indicates a highly activated intercage motion, which is confirmed by the Arrhenius plot of Figure 4.

Figure 5 reports the occupancy probability density $p(z)$ along the z axis inside the LTA cage for CH_4, C_2H_6, C_3H_6, and C_3H_8 in the temperature range 300−1200 K. The extremes in the Z coordinate ($Z = 0$, $Z \sim 12$) correspond to the 8-ring windows connecting cages, while the middle point ($Z \simeq 6$) refers to the cavity center. At the lower simulation temperature of 300 K, methane and ethane reside in well-defined zones of the cage, in positions with relative maxima in the probability density plots. As the temperature increases, the occupancy density gets smoother, with local maxima being displaced in favor of less localized distributions. This leveling of the intracage energy surface will produce a higher probability to sample new intracage regions, raising the probability to surmount the free energy barrier and thus increasing the net diffusivity of the guest

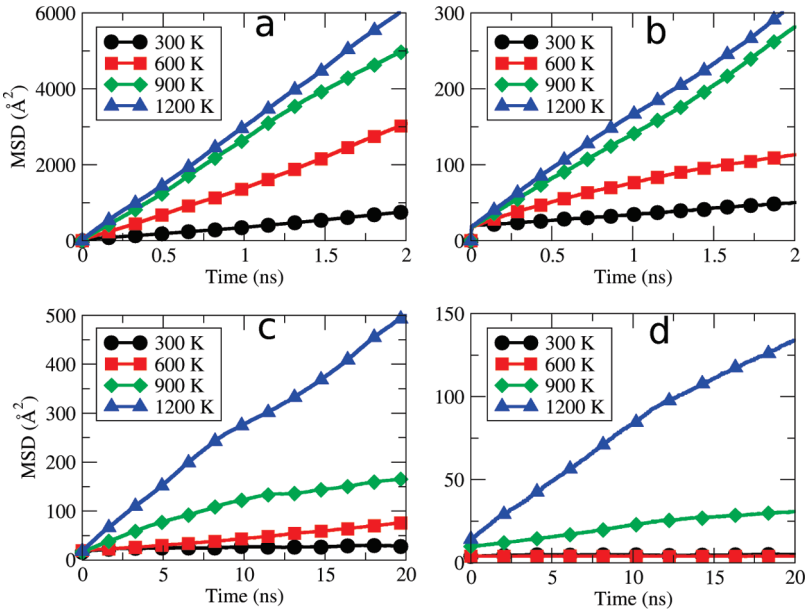

Figure 6. MSD plots for (a) methane, (b) ethane, (c) propene, and (d) propane adsorbed in Si-IHW zeolite at various temperatures.

molecule. The picture is very similar for ethane, although the density distribution plot shows less specific residence zones. In the case of propylene, we observe a certain degree of ordering at the lower temperature of 300 K, which makes the regions between the windows and the center of the cages slightly advantageous energetically. The accommodation of the molecules moves to a wider range of locations as the temperature increases, as a consequence of the higher thermal degree of mobility acquired by the guest phase. Propane shows a dynamical behavior without preferential absorption regions, which is almost unaffected by temperature increments. In all cases, the extreme values, $P(0)$ and $P(12)$, are not zero, which means that window crossing events (intercage migration) are verified. We will come over to this point later.

The Arrhenius plot drawn in Figure 4 shows the values of calculated activation energies for the diffusive molecules within the Si-LTA framework. The plot for methane and ethane shows a zone that departs from the linear trend at higher temperatures. Nevertheless, we have used all the points obtained to calculate the activation energy, although having in mind that the result will only serve as a criterion to discuss qualitatively the role of the diffusional barriers. The calculated slopes and corresponding activation energy show an almost negligible constraint to methane intercage motion through the 8-ring windows of Si-LTA, amounting to 2.54 kJ/mol. The calculated Arrhenius activation energy of ethane shows an increase of only 0.42 kJ/mol with respect to methane. Although the difference in molecular size of the adsorbates is appreciable, the activation energy is not that marked, suggesting that the size of the window is large enough to allow the intercage motion of the adsorbates without a high energy penalty. The picture changes dramatically for propylene and propane, with activation energies of 7.6 and 21.8 kJ/mol, respectively. The activation energy of propylene increases 3 times with respect to methane, making clear the entropic selectivity of the connecting intercage 8-ring window with respect to adsorbate size. The activation energy goes up to 21.8 kJ/mol for propene, which amounts to a 3-fold increase with respect to propylene and a 9-fold increase compared with methane. The relatively small difference in molecular size between propylene and propane is enough to produce a dramatic increase in the energetic intercage crossing barrier, which confirms the potential of this type of framework to affect the long-range dynamics of the adsorbates based on a pure steric hindrance effect, which is especially noticeable for the case of propane and propylene.

TABLE 5: Calculated Self-Diffusion Coefficients for Methane, Ethane, Propene, and Propane in All Silica IHW Zeolite

	diffusion coefficient D_s (m²/s)			
temp	CH_4	C_2H_6	C_3H_6	C_3H_8
300 K	9.4×10^{-10}	4.0×10^{-11}	8.3×10^{-13}	
600 K	3.9×10^{-9}	1.1×10^{-10}	8.2×10^{-12}	7.0×10^{-14}
900 K	6.5×10^{-9}	3.2×10^{-10}	1.1×10^{-11}	2.7×10^{-12}
1200 K	7.7×10^{-9}	3.5×10^{-10}	5.6×10^{-11}	1.5×10^{-11}

Si-IHW Host−Guest Dynamics. MSDs for guest molecules in Si-IHW zeolite are reported in Figure 6 in the temperature range 300−1200 K. Similarly to Si-LTA, a continuous raising of the hindrance to the inter- and intracage motion with increasing guest molecular size is seen for this framework. Methane follows a spaced increase of MSD with temperature up to 900 K; however, at 1200 K, the gap between MSDs is shortened drastically. This behavior suggests that increasing thermal excitations will affect the long-range motion of the guest only up to some extent; beyond this thermal threshold, there is not an appreciable contribution to diffusion. This behavior also appears for ethane, which presents a similar short gap between 900 and 1200 K. The long-range displacement of all the guest molecules in this zeolite suggests a more restricted diffusion compared to Si-LTA, which can also be concluded from the diffusion coefficients presented in Table 5. Notice the time scale of Figure 6a, which is twice as large as the one in Figure 3a, with a MSD scale of about one-half of that for Si-LTA.

The one-dimensional probability density distributions along the Y coordinate, presented in Figure 7, will be helpful to shed some light on the diffusional features of this system. Figure 7a shows the distribution of methane along the axis of the 12-ring channel, showing clearly three regions with a high probability of finding the methane molecules. The probability distribution inside the channel does not change dramatically at higher temperatures, as we can still distinguish three well-defined regions of absorption. This pattern can also be discerned for

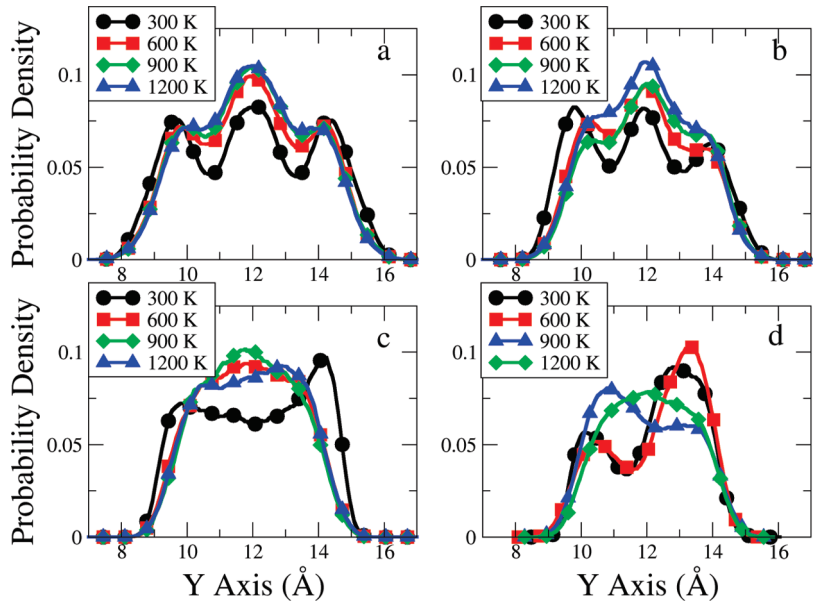

Figure 7. One-dimensional probability density distribution along the *Y* coordinate for (a) methane, (b) ethane, (c) propylene, and (d) propane center of mass in Si-IHW zeolite, and its evolution with temperature.

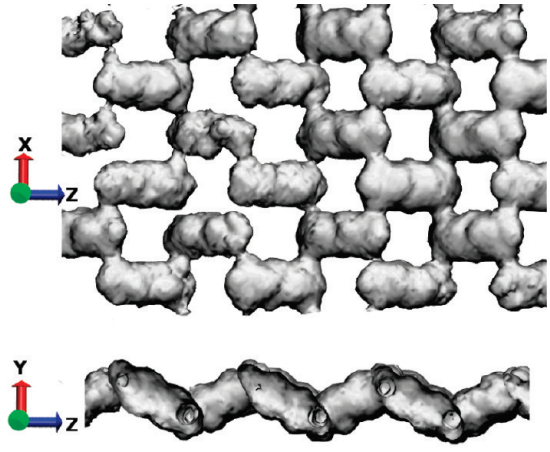

Figure 8. Occupancy volume map of methane center of mass while diffusing within the channels of Si-IHW.

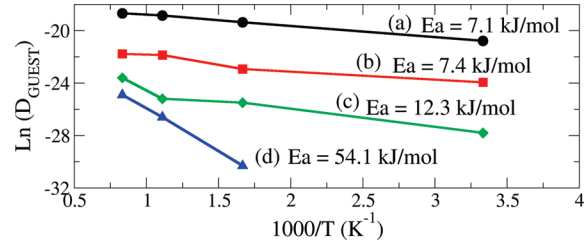

Figure 9. Arrhenius plots for (a) methane, (b) ethane, (c) propene, and (d) propane adsorbed in Si-IHW zeolite.

ethane in Figure 7b, where the same three peaks appear in the same regions as for methane, and the same temperature dependence, where the thermal excitations in the adsorbate push them to visit the more restricted areas of the channel. The occupancy volume map generated from the dynamics of the methane center of mass at high temperature is shown in Figure 8. This figure shows the zones with a low probability of finding the guest molecule, of course coinciding with the positions of the 8-ring windows, and the preferential adsorption zones inside the channels formed by the 12-ring system. The two-dimensional diffusion pattern followed by the guest is also evident from the planes drawn, with diffusion taking place along the *X* and *Z* coordinates and not along the *Y* axis.

The propylene and propane center of mass probability distribution shows a more restricted motion, with two well differentiated regions for the adsorption of the guest at the lower temperatures. As the temperature increases, the guest molecules begin to sample more frequently the central portion of the cages, producing a single and wider statistical distribution. In the particular case of propane, the level of constraint to the intracage motion is noticeable, as shown by the symmetrical distribution of configurations in the range 300−900 K. At 1200 K, the kinetic energy gained by the propane molecules is large enough to surmount the 12-member-ring intracage barrier, allowing a less restricted motion of the guest, which results in a single distribution of configurations along the cage. The calculated diffusion coefficients presented in Table 5 reflect numerically the increase in intercage diffusional hindrance presented in this system with respect to the previous case of Si-LTA, showing a decrease of 1 order of magnitude for the diffusion of methane and ethane.

Figure 9 shows the values of activation energies obtained for the guest molecules in Si-IHW. There exists a good linear Arrhenius trend in activation energies for methane and ethane in the Si-IHW framework along the temperature range, with small differences in activation energy between the smaller adsorbates. This suggests a similar picture to the one presented for Si-LTA, with almost negligible differences for the entropic restriction to methane and ethane intercage motion. However, the extent of the energetic barrier is 2−3 times larger compared with Si-LTA, which could be explained by two topologically influenced factors: the 8-ring window size and the differences in diffusional paths. The apparently small difference in 8-ring window size comparing Si-LTA and Si-IHW, which amounts to 0.6 Å, exerts a meaningful influence in the motion of the adsorbates. The second factor, that is, the diffusional path for intercage motion, also shows its influence. Figure 9 clearly shows the preferential adsorption sites for the adsorbates within Si-IHW. For the case of propylene and propane, activation energy values of 12.3 and 54.1 kJ/mol are calculated, respectively. There is a 5 kJ/mol increment of activation energy with respect to ethane, which reflects the effect of the adsorbate

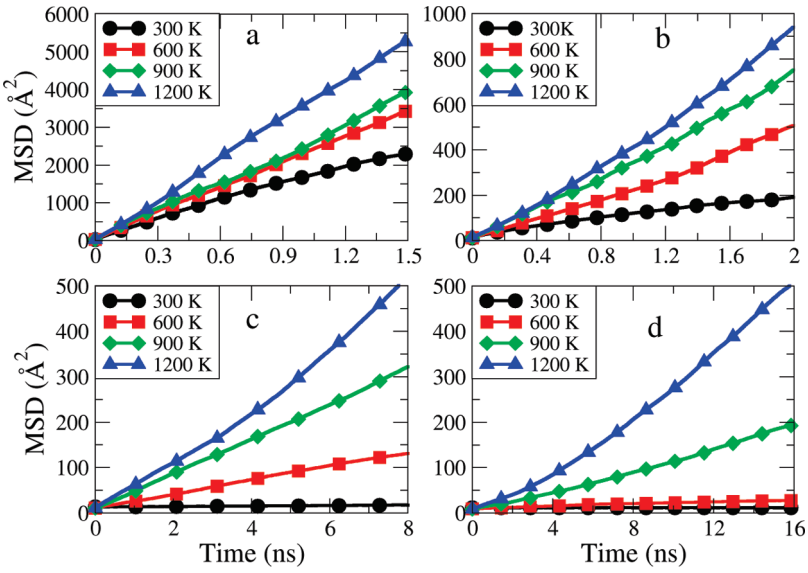

Figure 10. MSD plots for (a) methane, (b) ethane, (c) propene, and (d) propane adsorbed in Si-ITE zeolite at various temperatures.

TABLE 6: Calculated Self-Diffusion Coefficients for Methane, Ethane, Propene, and Propane in All Silica ITE Zeolite

	diffusion coefficient D_s (m^2/s)			
temp	CH_4	C_2H_6	C_3H_6	C_3H_8
300 K	7.4×10^{-9}	4.3×10^{-10}	3.4×10^{-12}	1.0×10^{-14}
600 K	1.1×10^{-8}	1.2×10^{-9}	7.0×10^{-11}	5.7×10^{-12}
900 K	1.3×10^{-8}	1.8×10^{-9}	2.1×10^{-10}	5.9×10^{-11}
1200K	1.8×10^{-8}	2.3×10^{-9}	3.4×10^{-10}	1.6×10^{-10}

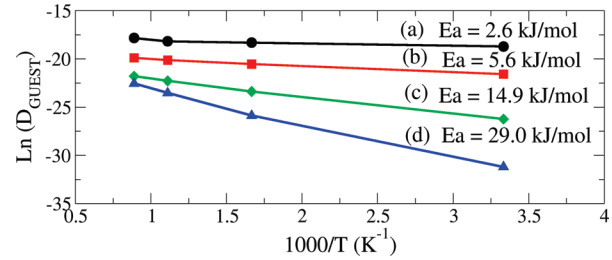

Figure 11. Arrhenius plot for (a) methane, (b) ethane, (c) propene, and (d) propane adsorbed in Si-ITE zeolite at various temperatures.

molecular size on the intercage mobility for this adsorbate. The energetic barrier rises up to 54 kJ/mol for propane, a 4−5-fold increment with respect to propylene, thus quantifying the energetic penalty due to the 8-ring barrier and the more constrained diffusion path through the framework.

Si-ITE Host−Guest Dynamics. Long-range motion of methane, ethane, propene, and propane adsorbed in Si-ITE zeolite is depicted in Figure 10. For methane and ethane, the time scales represented make the more restrictive diffusive environment of zeolite Si-ITE when compared with Si-LTA immediately clear, as suggested by the length of the MSDs. For methane in Si-ITE, the MSDs show a more than 2-fold reduction in length, as is also the case for ethane, where the decrease in MSD is of about 3 times at the higher temperature of 1200 K. The topology of Si-ITE only allows the motion of diffusants through one coordinate which is reflected in the values of the diffusion coefficients presented in Table 6. This effect, which is quantified in the parameter N_t in eq 1, reflects the allowed long-range translational degrees of freedom of the adsorbate inside the porous framework. The unidimensional diffusive path in this structure limits the movement of the diffusant; thus, when comparing with methane and ethane in Si-LTA, we see slightly larger values of self-diffusion coefficients in Si-ITE, which are also evident when we compare the diffusion coefficients of propene and propane. Figure 12 shows the one-dimensional diffusion character of this framework. The occupancy surface created by the methane center of mass clearly shows the bottlenecks formed at the 8-ring window positions and the less restricted zones visited by the guest inside the cavities.

The activation energies calculated for the guest phase in this system, depicted in Figure 11, show a good linear behavior up to 1200 K for methane and ethane, with E_a = 2.6 kJ/mol and E_a = 5.6 kJ/mol, respectively. This behavior contrasts with the almost equal activation energies calculated for methane/ethane in Si-LTA and Si-IHW, here doubling the energetic barrier imposed by the 8-ring intercage connecting path. The calculated activation energy for methane is similar to that of the smaller adsorbate in Si-LTA, whereas the value for ethane is twice as large. The activation energy of ethane inversely correlates with increasing 8-ring window size Si-LTA (4.1 Å - 2.96 kJ/mol) > Si- ITE (3.8 Å - 5.6 kJ/mol) > Si-IHW (3.5 Å - 7.4 kJ/mol), which nicely shows the influence of the changing framework intercage bottleneck on the same adsorbate. This trend is also evident for all of the adsorbates, with an evident increase in the level of activation energy also correlated with the guest kinetic size. The difference in activation energy for propylene, for instance, changes as Si-LTA (4.1 Å - 7.6 kJ/mol) > Si- ITE (3.8 Å - 14.9 kJ/mol) ≃ Si-IHW (3.5 Å - 12.3 kJ/mol). There is a close to 2-fold increase between the activation energies in Si-LTA and Si-ITE/Si-IHW, thus showing the higher level of intercage energy barrier for the larger adsorbate. This trend is also followed by propane, with 8-ring window size to activation energy following the sequence Si-LTA (4.1 Å - 21.8 kJ/mol) > Si-ITE (3.8 Å - 29.0 kJ/mol) > Si-IHW (3.5 Å - 54.1 kJ/mol). The calculated values of activation energy increase quite dramatically for propane, going up to 54 kJ/mol in Si-IHW, almost twice the value calculated for the same adsorbate in Si-ITE.

Experimentally obtained diffusion coefficients and activation energies for methane, ethane, and propane in zeolite 5A are presented for comparison with our calculations in Table 7. Zeolite 5A features a structure with 8-ring windows of about the same dimensions as its purely siliceous counterpart.

TABLE 7: Experimental Self-Diffusion Coefficients (D_s) and Activation Energies (AE) for Methane, Ethane, Propene, and Propane in 5A Zeolite[a]

	CH_4			C_2H_6			C_3H_8		
zeolite	technique	D_s (m^2/s)	AE (kJ/mol)	technique	D_s (m^2/s)	AE (kJ/mol)	technique	D_s (m^2/s)	AE (kJ/mol)
5A	neutron diff.	6.0×10^{-10}		ZLC	3.0×10^{-11}	6.7	NMR(PFG)	2.0×10^{-13}	
	NMR(PFG)	$\sim 10^{-9}$	4	NMR(PFG)	6.0×10^{-11}	6.0	grav. uptake	2.0×10^{-13}	14.5
							freq response	2.0×10^{-13}	
Si-LTA	300 K	5.9×10^{-9}	2.5	300 K	4.8×10^{-10}	3.0	600 K	4.0×10^{-12}	21.8
Si-IHW	300 K	9.4×10^{-10}	7.1	300 K	4.0×10^{-11}	7.4	600 K	7.0×10^{-14}	54.1
Si-ITE	300 K	7.4×10^{-9}	2.6	300 K	4.3×10^{-10}	5.6	300 K	1.0×10^{-14}	29.0

[a] The experimental values are taken at 300 K; further details are given in the original reference.[38]

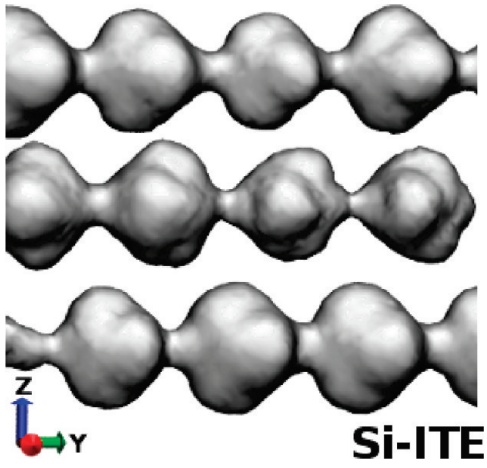

Figure 12. Occupancy volume map of methane center of mass while diffusing within the channels of Si-ITE.

Experimental values are taken from the data collected by Karger and Ruthven.[38] The activation energies calculated from experiments for zeolite 5A are comparable to our calculations, although the values for propane are much lower in comparison. This discrepancy can be expected, as the experimental technique suffers inherent limitations due to several factors, for instance, the degree of mobility of the different adsorbates which could reach the sensitivity limits of the measurement device. Nevertheless, the comparison with experimental data gives us a good level of confidence, as magnitudes of the properties calculated are in close agreement.

Comparison of Diffusional Features in Si-LTA, Si-IHW, and Si-ITE. Figures 9 and 12 show the diffusional path followed by methane at high temperature inside the Si-IHW and Si-ITE frameworks, respectively. The two-dimensional character of diffusion in zeolite Si-IHW is clearly seen in the *XZ* plane projection, with bottlenecks at the positions of the 8-ring windows and stretched zones around the 12-ring channels. The displacement of the guest on the *YZ* plane is shown to highlight the fact that diffusion along the *Y* coordinate is forbidden in this structure. The one-dimensional diffusive path of methane, which is equally representative for the other guest molecules, in Si-ITE is drawn in Figure 12. The bottlenecks represent, as in the case of Si-IHW, the 8-ring window positions, and the occupancy surface map obtained from the dynamics of the guest center of mass allows one to see the shape of the cages. The comparison between framework critical window size, guest self-diffusion coefficient, and Arrhenius activation energy at 600 K for methane, ethane, and propene is presented in Table 8. The 600 K temperature point was chosen for the comparison because this temperature provides enough intercage motion for C1−C3 hydrocarbons. We have defined the critical window size as a topological descriptor for each zeolite structure. It can

TABLE 8: Comparison of 8-Ring Critical Window Size (Smallest O−O Distance), Self-Diffusion Coefficients (D_s), and Arrhenius Activation Energies (AE) for Methane, Ethane, and Propene in All Silica Zeolites at 600 K

		D_s (m^2/s), AE (kJ/mol)		
framework	critical window size (Å)	CH_4	C_2H_6	C_3H_6
Si-LTA	4.1	6.1×10^{-9}, 2.5	4.3×10^{-10}, 2.9	5.6×10^{-11}, 7.6
Si-ITE	3.8	1.1×10^{-8}, 2.6	1.2×10^{-9}, 5.6	7.0×10^{-11}, 14.9
Si-IHW	3.5	3.9×10^{-9}, 7.1	1.1×10^{-10}, 7.4	8.2×10^{-12}, 12.3

TABLE 9: Comparison of 8-Ring Critical Window Size (Smallest O−O Distance), Self-Diffusion Coefficients, and Arrhenius Activation Energies (AE) for Propene and Propane in All Silica Zeolites at 1200 K

		D_s (m^2/s), AE (kJ/mol)	
framework	critical window size (Å)	C_3H_6	C_3H_8
Si-LTA	4.1	1.5×10^{-10}, 7.6	3.8×10^{-11}, 21.8
Si-ITE	3.8	3.4×10^{-10}, 14.9	1.6×10^{-10}, 29.9
Si-IHW	3.5	5.6×10^{-11}, 12.3	1.5×10^{-11}, 54.1

be seen that the decreasing trend in zeolite critical window size correlates directly with the self-diffusion coefficients for the guest, which shows the intercage mobility penalty due to the reduced size in critical window opening. Likewise, the activation energy variation allows one to see the same type of correlation, with higher activation energy values for the framework with lower critical window sizes and higher guest size.

On the other hand, the two C3 hydrocarbons considered here deserve a separate analysis, because a similar comparison as the one presented above would show no correlation with critical window size. Propene and propane high temperature self-diffusion coefficient, activation energy, and window critical size are shown separately in Table 9. Propene shows an increase in activation energy correlated with framework 8-ring window diameter, with the lowest value for Si-LTA and a 2-fold increase for Si-IHW and Si-ITE, which show very similar values. Self-diffusion coefficients are in the same order of magnitude for the three frameworks, with higher values for Si-ITE. However, correlations extracted from propane dynamics related to framework critical diameter are more difficult to assert. This is evident from the discontinuity in the trend of self-diffusion coefficient and activation energy for propane in Si-ITE, which are higher than that for Si-LTA, which features a larger window opening size. This fact shows that when the guest kinetic diameter is much closer to the window openings other features of the guest and framework start to play an important role. In this case, we rationalize the lack of correlation between guest self-diffusion coefficient and framework window size in terms of the dimensionality and topology of the framework. The fact that propane shows the highest self-diffusion coefficient in Si-ITE is due to the one-dimensional character of the diffusion path inside the framework, which will tend to concentrate the

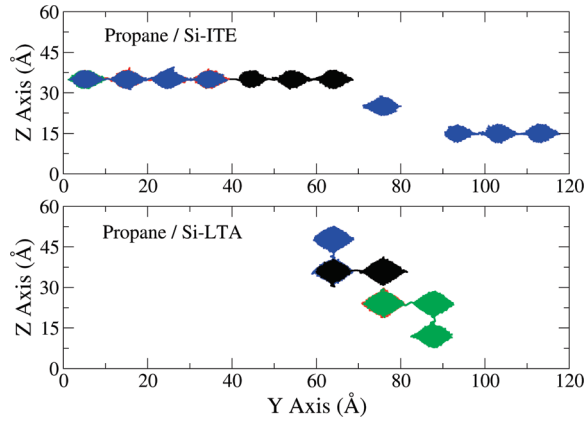

Figure 13. Diffusion path followed by propane center of mass while diffusing in Si-ITE (top) and Si-LTA (bottom) at 1200 K.

movement of the guest toward only one coordinate. The confinement effect in nanoporous materials suggested by Derouane,[39–43] and recently reviewed by Sastre and Corma,[44] nicely fits in this case as the size of the guest starts being large enough to feel the effect of the surrounding forcefield in a symmetric way, thus increasing the probability of being in the most favorable position (center of the cage) and with the most adequate conformation for the intercage jumping process to occur.

In spite of the larger window size of Si-LTA, compared with Si-ITE, propene self-diffusion turns out to be slower, due to the existence of preferential energy sites inside the Si-LTA cage which lowers the probability of finding the molecule in high probability intercage-jumping regions. This behavior is represented in Figure 13, showing the path followed by propane while diffusing inside Si-ITE and Si-LTA. The larger number of guest intercage jumps within Si-ITE compared with Si-LTA is clear, as well as the more restricted intracage motion in Si-ITE.

In the case of Si-IHW, with channels running in the z axis connected perpendicularly in the x coordinate through 8-ring windows, there is a less expedite path for the diffusion of propane, thus increasing the energetic barrier and decreasing the chance for intercage/interchannel movements of the guest. This criteria explains in a qualitative way the intercage motion of the larger size adsorbates, although the fact that we are comparing thermally highly activated systems should be emphasized. The statistical uncertainty in diffusional coefficients for propene and propane at low temperatures precludes the possibility to extract meaningful correlations between diffusion properties, window size, and dimensionality of the framework at low intercage mobility. However, efforts in this direction are being made by implementing a methodology based on rare event approaches, specifically the dynamically corrected transition state theory, which will allow the calculation of statistically meaningful self-diffusion coefficients.[16,45,46] Also, for a better comparison with experimental diffusion measurements, the role of the surface resistances is being accounted for and will be the subject of a forthcoming publication.

Conclusions

MD calculations have been carried out to study the short- and long-range motion of C1−C3 hydrocarbons, with increasingly larger kinetic diameters, adsorbed in three different pure silica 8-ring zeolite frameworks: ITQ-29(Si-LTA), ITQ-32(Si-IHW), and ITQ-3(Si-ITE). The chosen porous structures feature three-dimensional diffusion paths in the case of Si-LTA, two-dimensional in the case of Si-IHW, and two-dimensional for Si-ITE, although only one of the diffusion paths in the latter framework allows the intercage translational motion for the hydrocarbons studied (pseudo 1D). The zeolite framework was simulated using the BKS forcefield allowing full flexibility, thus including the dynamic interaction between the exposed oxygen atoms in the internal surface of the porous system and the flexible guest phase. For the lower kinetic size adsorbates, i.e., methane and ethane, it was observed that the simulation approach allows one to calculate the intra- and intercage dynamics in statistically meaningful time and length ranges, whereas for the larger size guest molecules the analysis of intercage motion is limited to higher temperatures. The molecular motion was analyzed by calculating MSDs of the adsorbed hydrocarbons as well as the occupation probability density of the center of mass of the guest.

Self-diffusion coefficients show a decreasing trend correlated with increasing guest kinetic diameter sizes and decreasing zeolite critical window size, confirming experimental measurements on the diffusion hindrance exerted by the 8-ring window present in the structure of the framework. Guest translational long-range motion is shown to be highly influenced for the topological features of the framework, with the dimensionality of the diffusion paths presented by the framework posing a noticeable influence. The influence of the 8-ring window size of the framework is clearly seen by comparing the diffusional coefficients of methane, ethane, and propene, giving larger values for the wider window opening of Si-LTA and lower for the somewhat elongated conformation of the Si-IHW zeolite. This trend is confirmed by looking at the activation energies, which also show an increasing tendency in the order Si-LTA, Si-ITE, and Si-IHW. Propane and propene inter- and intracage motion comparison allows one to see a somewhat different picture, with a higher intercage motion for propane in Si-ITE, which precludes the rationalization of the self-diffusion coefficient based on the critical size of the windows. Thus, the framework topology will dictate the diffusional behavior of the guest, which can be clearly appreciated by the differences in activation energies and self-diffusional constants calculated.

ITQ-3 shows intermediate activation energies, with a ratio $AE^{Propylene}/AE^{Propane} \sim 0.5$, and high intracrystalline self-diffusion coefficients for propane/propylene; thus, in a hypothetical kinetic separation process, it will allow fast separation but low selectivity. On the other hand, ITQ-32 shows the largest difference in activation energy, with a ratio $AE^{Propylene}/AE^{Propane} \sim 0.23$, and the lowest self-diffusion coefficients between propane/propylene, so we could predict a high degree of selectivity in a slow separation process for this material. These two zeolite−guest systems show the existing trade-off between high diffusional differentiation and selectivity recently highlighted by Hedin et al.,[20] where commercial considerations will have the last word at the moment of choosing a certain framework type for a specific separation process.

Further efforts toward a deeper description of the diffusional properties of adsorbates in zeolites with 8-ring windows, including the loading dependence of self-diffusional coefficients, the consideration of more statistically rigorous methods for the calculation of rare events, as well as considering the influence of diffusional barriers posed by the surface topology, are being made and will be the subject of a forthcoming publication.

Acknowledgment. Funding through Ministerio de Ciencia e Innovación (Project MAT2007-64682) and computing time from Red Española de Supercomputación are gratefully acknowl-

edged. A.F.C. thanks the Instituto de Tecnología Química UPV-CSIC for a research fellowship.

References and Notes

(1) Corma, A. *J. Catal.* **2003**, *216*, 298–312.
(2) Song, L.; Sun, Z.; Duan, L.; Gui, J.; McDougall, G. S. *Microporous Mesoporous Mater.* **2007**, *104*, 115–128.
(3) Li, Z.; Johnson, M. C.; Sun, M.; Ryan, E. T.; Earl, D. J.; Maichen, W.; Martin, J. I.; Li, S.; Lew, C. M.; Wang, J.; Deem, M. W.; Davis, M. E.; Yan, Y. *Angew. Chem., Int. Ed.* **2006**, *45*, 6329–6332.
(4) Sun, J.; Bonneau, C.; Cantin, A.; Corma, A.; Diaz-Cabanas, M. J.; Moliner, M.; Zhang, D.; Li, M.; Zou, X. *Nature* **2009**, *458*, 1154–1157.
(5) Palomino, M.; Cantín, A.; Corma, A.; Leiva, S.; Rey, F.; Valencia, S. *Chem. Commun.* **2007**, 1233–1235.
(6) Olson, D. H.; Camblor, M. A.; Villaescusa, L. A.; Kuehl, G. H. *Microporous Mesoporous Mater.* **2004**, *67*, 27–33.
(7) Barrett, P. A.; Boix, T.; Puche, M.; Olson, D. H.; Jordan, E.; Koller, H.; Camblor, M. A. *Chem. Commun.* **2003**, 2114–2115.
(8) Camblor, M. A.; Corma, A.; Lightfoot, P.; Villaescusa, L. A.; Wright, P. *Angew. Chem., Int. Ed.* **1997**, *36*, 2659–2661.
(9) Cantin, A.; Corma, A.; Leiva, S.; Rey, F.; Rius, J.; Valencia, S. *J. Am. Chem. Soc.* **2005**, *127*, 11560–11561.
(10) Ruthven, D. M.; Reyes, S. *Microporous Mesoporous Mater.* **2007**, *104*, 59–66.
(11) Corma, A.; Rey, F.; Rius, J.; Sabater, M. J.; Valencia, S. *Nature* **2004**, *431*, 287–290.
(12) Demontis, P.; Suffritti, G. B. *J. Phys. Chem. B* **1997**, *101*, 5789–5793.
(13) Fritzsche, S.; Haberlandt, R.; Hofmann, G.; Kärger, J.; Heinzinger, K.; Wolfsberg, M. *Chem. Phys. Lett.* **1997**, *265*, 253–258.
(14) Haberlandt, R. *Thin Solid Films* **1998**, *330*, 34–45.
(15) Astala, R.; Auerbach, S. M.; Monson, P. A. *J. Phys. Chem. B* **2004**, *108*, 9208–9215.
(16) Beerdsen, E.; Smit, B.; Dubbeldam, D. *Phys. Rev. Lett.* **2004**, *93*, 248301.
(17) Nagumo, R.; Takaba, H.; Nakao, S. *J. Phys. Chem. C* **2008**, *112*, 2805–2811.
(18) Corma, A.; Kärger, J.; Krause, C. *Diffusion Fundamentals* **2005**, *2*, 87.1–87.2.
(19) Hedin, N.; DeMartin, G. J.; Strohmaier, K. G.; Reyes, S. C. *Microporous Mesoporous Mater.* **2007**, *98*, 182–188.
(20) Hedin, N.; De Martin, G. J.; Roth, W. J.; Strohmaier, K. G.; Reyes, S. C. *Microporous Mesoporous Mater.* **2008**, *109*, 327–334.
(21) Kärger, J. *Microporous Mesoporous Mater.* **2008**, *109*, 715–717.
(22) Liu, B.; Smit, B.; Rey, F.; Valencia, S.; Calero, S. *J. Phys. Chem. C* **2008**, *112*, 2492–2498.
(23) Combariza, A. F.; Sastre, G.; Corma, A. *J. Phys. Chem. C* **2009**, *113*, 11246–11253.
(24) Baerlocher, C.; McCusker, L.; Olson, D. H. *Atlas of Zeolite Framework Types*, 6th ed.; Elsevier: Amsterdam, The Netherlands, 2007.
(25) Rohrbaugh, R. H.; Jurs, P. *Anal. Chim. Acta* **1987**, *199*, 99–109.
(26) Smith, W.; Yong, C. W.; Rodger, P. M. *Mol. Simul.* **2002**, *28*, 385–471.
(27) Demontis, P.; Suffritti, G. B. *Microporous Mesoporous Mater.* **2009**, *125*, 160–168.
(28) Jakobtorweihen, S.; Lowe, C. P.; Keil, F. J.; Smit, B. *J. Chem. Phys.* **2007**, *127*, 024904.
(29) Frenkel, D.; Smith, B. *Understanding Molecular Simulation*; Academic Press: New York, 2002.
(30) Shell, M. S.; Panagiotopoulos, A.; Pohorille, A. In *Free Energy Calculations*; Chipot, C., Pohorille, A., Eds.; Springer: New York, 2007; pp 77−116 (Methods based on probability distributions and histograms).
(31) Ewald, P. P. *Ann. Phys.* **1921**, *64*, 253.
(32) van Beest, B. W. H.; Kramer, G. J.; van Santen, R. A. *Phys. Rev. Lett.* **1990**, *64*, 1955–1958.
(33) Oie, T.; Maggiora, T. M.; Christopherssen, R.; Duchamp, D. J. *Int. J. Quantum Chem., Quantum Biol. Symp.* **1981**, *8*, 1.
(34) Catlow, C. R. A.; Freeman, C. M.; Vessal, B.; Tomlinson, S. M.; Leslie, M. *J. Chem. Soc., Faraday Trans.* **1991**, *87*, 1947–1950.
(35) Llopis, F.; Sastre, G.; Corma, A. *J. Catal.* **2004**, *227*, 227–241.
(36) Krishna, R.; van Baten, J. M. *Chem. Eng. Technol.* **2007**, *30*, 1235.
(37) Krishna, R.; van Baten, J. M. *Chem. Eng. Technol.* **2006**, *29*, 1429.
(38) Kärger, J.; Ruthven, D. M. *Diffusion in Zeolites and Other Microporous Solids*; John Wiley and Sons: New York, 1992.
(39) Derouane, E. *J. Catal.* **1986**, *100*, 541–544.
(40) Derouane, E. *Chem. Phys. Lett.* **1987**, *142*, 200–204.
(41) Derouane, E.; André, J.-M.; Lucas, A. *Chem. Phys. Lett.* **1987**, *137*, 336–340.
(42) Derouane, E. G.; Andre, J. M.; Lucas, A. A. *J. Catal.* **1988**, *110*, 58–73.
(43) Derycke, I.; Vigneron, J. P.; Lambin, P.; Lucas, A. A.; Derouane, E. G. *J. Chem. Phys.* **1994**, *94*, 4620–4627.
(44) Sastre, G.; Corma, A. *J. Mol. Catal.* **2009**, *305*, 3–7.
(45) Auerbach, S. M. *Int. Rev. Phys. Chem.* **2000**, *19*, 155–198.
(46) Beerdsen, E.; Dubbeldam, D.; Smit, B. *Phys. Rev. Lett.* **2005**, *95*, 164505.

JP102262N